Ultracool dwarfs candidates based on 6 yr of the Dark Energy Survey data

M. dal Ponte [1,2]★ B. Santiago,[1,2]★ A. Carnero Rosell [2,3,4]★ L. De Paris,[1] A. B. Pace [5] K. Bechtol,[6] T. M. C. Abbott,[7] M. Aguena,[2] S. Allam,[8] O. Alves,[9] D. Bacon,[10] E. Bertin,[11,12] S. Bocquet,[13] D. Brooks,[14] D. L. Burke,[15,16] M. Carrasco Kind,[17,18] J. Carretero,[19] C. Conselice,[20,21] M. Costanzi,[22,23,24] S. Desai,[25] J. De Vicente,[26] P. Doel,[14] S. Everett,[27] I. Ferrero,[28] B. Flaugher,[8] J. Frieman,[8,29] J. García-Bellido,[30] D. W. Gerdes,[31,9] R. A. Gruendl,[17,18] D. Gruen,[13] G. Gutierrez,[8] S. R. Hinton,[32] D. L. Hollowood,[33] D. J. James,[34] K. Kuehn,[35,36] N. Kuropatkin,[8] J. L. Marshall,[37,38] J. Mena-Fernández,[26] F. Menanteau,[17,18] R. Miquel,[19,38] R. L. C. Ogando,[39] A. Palmese,[40] F. Paz-Chinchón,[17,41] M. E. S. Pereira,[42] A. A. Plazas Malagón,[43] A. Pieres [2,39] M. Raveri,[44] M. Rodriguez-Monroy,[26] E. Sanchez,[26] V. Scarpine,[8] M. Schubnell,[9] I. Sevilla-Noarbe,[26] M. Smith,[45] M. Soares-Santos,[9] E. Suchyta,[46] M. E. C. Swanson,[19] G. Tarle,[9] D. Thomas,[10] C. To,[47] N. Weaverdyck[9,48] and (DES Collaboration)

Affiliations are listed at the end of the paper

ABSTRACT

We present a sample of 19 583 ultracool dwarf candidates brighter than z $\leq$23 selected from the Dark Energy Survey DR2 coadd data matched to VHS DR6, VIKING DR5, and AllWISE covering $\sim$ 480 deg^2. The ultracool candidates were first pre-selected based on their (i–z), (z–Y), and (Y–J) colours. They were further classified using a method that compares their optical, near-infrared, and mid-infrared colours against templates of M, L, and T dwarfs. 14 099 objects are presented as new L and T candidates and the remaining objects are from the literature, including 5342 candidates from our previous work. Using this new and deeper sample of ultracool dwarf candidates we also present: 20 new candidate members to nearby young moving groups and associations, variable candidate sources and four new wide binary systems composed of two ultracool dwarfs. Finally, we also show the spectra of 12 new ultracool dwarfs discovered by our group and presented here for the first time. These spectroscopically confirmed objects are a sanity check of our selection of ultracool dwarfs and photometric classification method.

Key words: surveys – brown dwarfs – stars: low-mass.

1 INTRODUCTION

Ultracool dwarfs (UCDs) are very cool (T_{eff} < 2700 K), low mass (M < 0.1 $M_\odot$) objects, ranging from spectral type M7 and later. They include both very low mass stars and brown dwarfs. Brown dwarfs are not massive enough ($\sim$ 0.072 $M_\odot$) to burn hydrogen in their core. Therefore, they continue to cool and dim over time across spectral types M, L, T, and Y (Kirkpatrick et al. 1999; Cushing et al. 2011). Without sustained hydrogen fusion, there is a degeneracy between mass, age, and luminosity. Their spectra are characterized by the effects of clouds and molecular absorption bands. For the L dwarfs, the spectra in the red optical is characterized by the weakening of TiO and VO, strengthening of FeH, CrH, H$_2$O, and alkali metals such Na I, K I, Cs I, Rb I (Kirkpatrick et al. 1999). The mid infrared spectra are similar to M dwarfs, with H$_2$O and CO as the most prominent bands

along with the presence of clouds in the photosphere (Burgasser et al. 2002b). The transition sequence to the T dwarfs is characterized by the disappearance of clouds from the photosphere, leading to relatively bluer colours in the near-infrared (NIR) compared to the L sequence. Their spectra is characterized by strong absorption features of H$_2$O, CH$_4$, and CIA H$_2$ (Burgasser et al. 2002a).

Despite UCDs being a very common type of object in the Galaxy, roughly 1/6 of the local stellar population by number density, they are very difficult to detect at larger distances due to their faint luminosities. Large samples of UCDs from wide-field imaging surveys [eg. Two-Micron All-Sky Survey (2MASS; Skrutskie et al. 2006), Deep Near Infrared Survey of the Southern Sky (DENIS; Epchtein et al. 1997), UKIRT Infrared Deep Sky Survey (UKIDSS; Lawrence et al. 2007), Wide-field Infrared Survey Explorer (WISE; Wright et al. 2010), VISTA Hemisphere Survey (VHS; McMahon et al. 2013)] have been discovered and revealed many important features about the ultracool dwarfs population. However, the census is still heterogeneous and shallow. The accurate identification and classification of ultracool dwarfs in wide deep ground-based surveys

using only photometry enables the creation of homogeneous samples without relying on extensive spectroscopic campaigns. These samples are essential to measuring the luminosity and mass functions (Cruz et al. 2007; Bochanski et al. 2010) of the ultracool dwarfs in the Galaxy, the disk scale height (Ryan et al. 2005; Carnero Rosell et al. 2019; Sorahana, Nakajima & Matsuoka 2019), the frequency of close and wide binaries (Luhman 2012; Dhital et al. 2015; Fontanive et al. 2018), and the kinematics (Faherty et al. 2010, 2012; Smith et al. 2014; Best et al. 2018).

Taking advantage of the Dark Energy Survey (DES) depth in the optical bands *i*, *z*, and *Y*, it is possible to select a large homogeneous sample of UCD candidates to greater distances. Carnero Rosell et al. (2019) were able to select a sample of 11 745 L and T dwarf candidates using the first 3 yr of the DES along with VHS and AllWISE (Cutri et al. 2013) data. Here we expand the search for ultracool dwarfs candidates using the full 6 yr of DES observations. Comparing to Carnero Rosell et al. (2019), the DES data are now photometrically deeper, with more reliable/precise photometry. This will allow us to probe fainter candidates, increasing the previous samples of L and T dwarfs. Besides, we have now available a sky coverage of almost the entire DES footprint, whereas in Carnero Rosell et al. (2019) we only had ∼ 2400 deg². This is due to the new data releases of VHS and VIKING surveys that are also used in the analyses.

The paper outline is as follows. In Section 2 we present the photometric data used in this work. In Section 3 we present the updated colour templates for M dwarfs and UCDs and the colour cuts used to pre-select our candidates. In Section 4 we discuss the photometric classification methodology, where we estimate a spectral type for each target using only their photometry. In Section 5 we compare our photo-type to those of known candidates from the literature and discuss the contamination by extragalactic sources. In Section 6, we present several uses for our L and T dwarf candidates: (i) new young moving group (YMG) and association candidate members; (ii) photometric variable sources; (iii) new binary systems constituted by two ultracool dwarfs. In Section 7 we show the spectra of 12 new ultracool dwarfs presented previously in the Carnero Rosell et al. (2019) catalogue that supports our selection of ultracool dwarfs and photometric classification method. Finally, in Section 8, we present our conclusions.

2 DATA

2.1 DES, VHS, VIKING, and AllWISE

DES is a ∼5000 deg² optical survey in the *grizY* bands that used the Dark Energy Camera (DECam; Flaugher et al. 2015). DECam is a wide-field (3 deg²) imager at the prime focus of the Blanco 4-m telescope at Cerro Tololo Inter-American Observatory (CTIO). DES observations started in September 2013 and were completed in January 2019, spanning nearly 6 yr.

DES DR2 is the assembled dataset from 6 yr of DES science operations, with data collected over 681 nights and which includes 691 million astronomical objects detected in 10 169 coadded image tiles of size 0.534 deg² produced from 76 217 single-epoch images. The estimated area loss to image defects, saturated stars, satellite trails, etc. is of ≃ 200 deg². After a basic quality selection, galaxy and stellar samples contain 543 million and 145 million objects, respectively. The typical depths (in AB system) as estimated from the magnitude at S/N = 10 in the coadd images are $g = 24.0$, $r = 23.8$, $i = 23.1$, $z = 22.13$, and $Y = 20.7$ (Abbott et al. 2021).

For the purpose of our work, we matched the DES DR2 catalogue to the VHS DR6, VIKING DR5 (Edge et al. 2013), and AllWISE catalogues using a positional matching radius of 2 arcsec, keeping only the best match, i.e, the nearest object found. The DES + VHS coverage area is around 4500 deg². The VHS survey is imaged with exposure time per coadded image of 120–240 seconds in *J* and 120 seconds in K_s. There is also partial coverage in the *H* band with an exposure time of 120 seconds. The median 5σ point source depths is $J_{AB} \sim 21.4$, $H_{AB} \sim 20.7$, and $K_{s,AB} \sim 20.3$. Since, by design, the VIKING and VHS footprints are complementary, we decided to use also the VIKING DR5 data in regions not covered by VHS. The DES + VIKING coverage is about 500 deg², providing along with VHS, almost the entire DES footprint. VIKING has a median depths at 5σ of $J_{AB} \sim 22.1$, $H_{AB} \sim 21.5$, and $K_{s,AB} \sim 21.2$ across all imaged regions (∼ 1350 deg²). Lastly, for the AllWISE survey we will use only *W*1 and *W*2 bands, which is >95 per cent complete for sources with *W*1 < 17.1 and *W*2 < 15.7 (in Vega system).

Some quality cuts were initially applied to the matched catalog, such as `IMAGFLAGS_ISO_i,z,Y = 0` from DES DR2 and `J,H,K_sppErrBits < 255`, to ensure that the object has not been affected by spurious events in the images in *i*, *z*, *Y*, *J*, *H* and K_s bands. We also imposed a magnitude limit cut of $z < 23$ (DES) and a simultaneous 5σ level detection in the *i*, *z*, *Y* (DES) and *J* (VHS + VIKING). We did not apply any standard star/galaxy separation because they are not as efficient for relatively nearby sources with significant signature of proper motions on their coadded DES images. In this work, we adopted the `PSF_MAG_i,z,Y` magnitude type from DES and `apermag3_J,H,Ks` from VHS and VIKING catalogues. Also, all DES magnitudes and colours are in the AB system and the VHS + VIKING and AllWISE magnitudes and colours are in the Vega system.

It is important to mention that for sources with significant proper motions, a matching radius of 2 arcsec may be too small. This matching radius will work except for the very nearby (< = 6 pc) or high-velocity (> 50 km s⁻¹) cases. Therefore, a small percentage of ultracool dwarfs will be missing from our catalogue due to this effect. The matching between DES data and others surveys provides a broad photometric baseline, spanning from the optical to the infrared. All these bands will be later used to construct empirical templates, perform the colour selection and photometrically estimate the spectral type of our UCDs candidates. The entire selection and classification process is summarized in Table 1 where every step is highlighted along with the corresponding section in this paper.

2.2 Known ultracool dwarfs

The sample from Best et al. (2020; hereafter B2020 sample) contains the most up-to-date compilation of ultracool dwarfs with spectroscopic confirmation. The complete sample has 2940 sources, with spectral type ranging from M3 to Y2. This compilation includes spectral types from optical and NIR. When both are available for a source, the authors recommend using optical types for M and L dwarfs and NIR types for T dwarfs, given that these are the spectral domains of the dominant features required for spectral classification in each case. From this catalogue there are 388 sources located in the DES footprint, and 292 of them are classified as L or T dwarfs. For the construction of the templates, we excluded objects flagged in the B2020 sample as unresolved binaries and sub-dwarfs. We first matched the B2020 sample of L and T dwarfs with the DES DR2 catalogue and found 227 objects in common. Since we have a small number of objects between the B2020 sample and DES, we decided to adopt only in this step a positional match of

Table 1. Steps used in this paper to select and classify L and T dwarfs using DES+VHS+VIKING + AllWISE.

Step	Description	Number of targets	Section
0	DES Y6 (DR2)	691 483 608	2.1
1	$z < 23$ $SNR_{z, Y} > 5\sigma$ IMAFLAGS_ISO_i,z,Y $= 0$ $(i–z)_{AB} > 1.20$ $(z–Y)_{AB} > 0.15$	602 366	2.1
2	Matching 2 arcsec DES +VHS + VIKING $(Y_{AB}–J_{Vega}) > 1.55$ $SNR_J > 5\sigma$ J, H, K_sppErrBits > 256	164 406	2.1
3	Matching 2 arcsec DES + AllWISE	76 184	3
4	Photo-Type classification $\geq$ L0	53 565	4
5	After removal of extragalactic contamination	19 449	5.2
6	Recover by proper motion criterion	141	5.3
7	From the literature	5484	5.4
8	New candidates	14 099	5.5

Note. First, a magnitude limit is imposed in the z band, quality cuts are applied to the data to remove spurious targets and colour cuts $(i–z)$, $(z–Y)$, and $(Y–J)$ are applied to select only the reddest objects. These are the sources that enter into the classification method. Next, we imposed that every object must have six or more bands and spectral type L0 or later. Then, extragalactic contamination is removed and the proper motion is assessed to recover objects erroneously assigned as extragalactic sources. Finally, we list candidates previously found in the literature and new ones.

3 arcsec. Every matched source was inspected visually using the DES image portal tool. The remaining 65 objects were eliminated in our selection due to quality cuts or for having a positional match beyond the limit. Then we matched B2020+DES DR2 with VHS DR6 and VIKING DR5 resulting in 185 objects in common. The 42 lost objects in the match between DES and VHS + VIKING are due to lack of data or positional match beyond 2 arcsec or the VHS+VIKING quality flag applied. Finally, we matched all the B2020 sample with a combination of VHS+VIKING + AllWISE, regardless of DES data, and we end up with 658 objects. We take these three steps in order to obtain as many objects as possible to construct our colour templates. In comparison with the sample of known ultracool dwarfs in Carnero Rosell et al. (2019), there are more 19 objects with DES magnitudes, 81 more in DES+VHS+VIKING, and 530 more in VHS+VIKING+AllWISE. Here, the difference between the samples with and without DES data is due to the limited area of the south where DES footprint is located. The combination of VHS+VIKING + AllWISE covers almost the entire southern hemisphere.

2.3 Known contaminants

There are two main types of sources that we consider as contaminants at this stage: M dwarfs and quasars at high redshift. In Carnero Rosell et al. (2019) we used a sample of 70 841 visually inspected M dwarfs from West et al. (2011). Here we use the Kiman et al. (2019) compilation of spectroscopic confirmed 73 473 M and 743 L or later dwarfs from SDSS constructed from West et al. (2011) and Schmidt et al. (2015, 2019). The match between Kiman et al. (2019) and DES DR2, VHS DR6, and AllWISE data resulted in 19 355 objects in common. This updated M dwarfs sample, with new DES photometry, is fundamental for the update of our colour templates,

used in the classification scheme. Regarding the quasars, we are now using the quasar catalogue from SDSS DR16 presented by Lyke et al. (2020). For this latter, we only kept objects with redshift $z > 4$. The reason is that the low-z quasars have much bluer colours than the UCDs and therefore are not relevant to our contamination analysis.

3 TEMPLATES AND COLOUR SELECTION

We updated our empirical colour templates using the samples of known M, L and T dwarfs described previously. The construction of the templates followed the same methodology described in Carnero Rosell et al. (2019). For the M dwarfs (M0–M9), we used the median colour for each spectral type as the template value. We demanded SNR $> 5\sigma$ in all bands and excluded objects that were $>2\sigma$ from the median. The median was then recalculated after these outliers were removed in an interative process until convergence. For the L and T dwarfs, because of the smaller number of objects, we fit a n order polynomial to each colour vs spectral type relation, using the least squares method. For $(i–z)$, $(J–K_s)$, $(H–K_s)$, and $(K_s–W1)$ an order 4 polynomial was used; $(Y–J)$ and $(W1–W2)$ an order 3 and $(z–Y)$ order 2 polynomial were used.

We re-estimated the intrinsic scatter for each colour index, assuming it to be the same for all spectral types. This intrinsic scatter is the spread in colour due to variations in metallicity, surface gravity, cloud cover, and also the uncertainty in the spectral classification. The procedure to estimate this intrinsic scatter followed the Skrzypek et al. (2015) prescription. We initially adopted a first guess of intrinsic scatter as 0.5 mag and added it in quadrature to the photometric errors to all templates. This new uncertainty was used to weight the points in the polynomial regression to the colour vs spectral type relation. Then, we re-estimated the intrinsic scatter as the variance of the best-fitting residuals with the rms value of the photometric errors subtracted in quadrature from it. This new value was taken as our intrinsic scatter for that colour index, irrespective of spectral type. Finally, we re-fitted the polynomial for L and T dwarfs, using the new intrinsic scatter. The intrinsic scatter values found with this method are the following: $\sigma_{i–z} = 0.34$, $\sigma_{z–Y} = 0.30$, $\sigma_{Y–J} = 0.37$, $\sigma_{J–H} = 0.32$, $\sigma_{H–Ks} = 0.30$, $\sigma_{Ks–W1} = 0.33$, $\sigma_{W1–W2} = 0.34$. These values are slightly smaller than those presented by Dupuy & Liu (2012) but more aligned with those presented recently in Kirkpatrick et al. (2021a). Even though there might be a systematic increase with spectral type, we will adopt a single value of 0.2 mag for each magnitude, corresponding to 0.3 mag for each colour index. These will later to be used to perform the spectral classification of our target sample.

The templates for the several colour indices as a function of the spectral type are shown in Fig. 1. Also shown are the templates presented in Carnero Rosell et al. (2019). In comparison to our previous templates, there are no significant changes for the M and L dwarfs. For the T dwarfs, specially late types, colour indices have changed typically by 0.1–0.2 mag, up to $\simeq 0.5$ mag in a couple of cases for T7 or later. This may be due to the clear increase in the number of objects that now contribute to the updated fit. The redder $J–H$ and $H–K_s$ colours around L4 and T0 types are a known trend caused by the effect of condensate clouds and the variability in the clouds properties. Also, there is a blueward trend for T2 to T7 types in $J–H$, $H–K_s$, and $K_s–W1$ due to the loss of the cloud decks and the onset of CH_4 absorption. However, this trend diminishes for the latest types as very little flux remains to be absorbed by CH_4 (Leggett et al. 2010). The scatter for the later T types in $H–K_s$ and $K_s–W1$ is due to the variations in metallicity and gravity. The template colours are shown in Table 2.
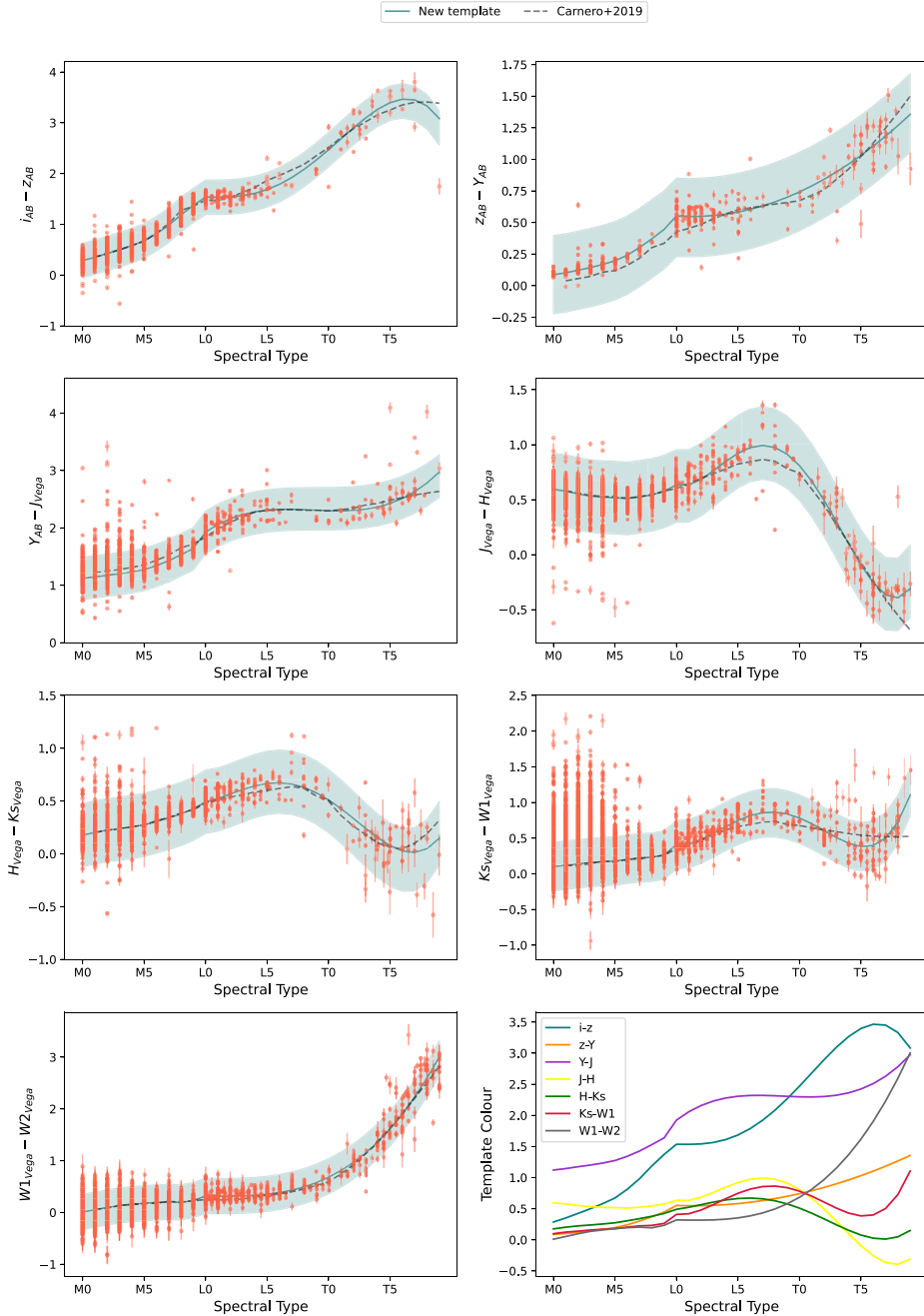
Figure 1. Colours as a function of the spectral type for the enlarged sample of known UCDs as described in the text. The dashed line indicates the new templates, as discussed previously in Section 3, and the solid line refers to the templates presented in Carnero Rosell et al. (2019). The light-shaded area corresponds to the intrinsic scatter of each colour. The last panel shows all the new updated templates for each colour indices used in this work.

For the colour selection of the UCDs, we follow the same methodology presented in Carnero Rosell et al. (2019). We analyse several colour–colour diagrams considering the UCDs and the contaminants samples presented earlier. The colour selection is meant to yield a sample of UCDs sources as complete as possible, at the expense of allowing some contamination by late-M dwarfs and extragalactic sources. The purity of our sample will be later improved using the photo-type classification (see Section 4). We applied an optical band cut ($i–z$) > 1.20, in order to remove the quasars, and also ($z–Y$) > 0.15 and ($Y–J$) > 1.55 to remove M dwarfs and other contamination sources. Fig. 2 shows the colour–colour diagrams where the colour

selection was applied for known contaminants, M dwarfs, and UCDs sources. Applying the colour selection discussed above, the initial sample has 164 406 sources in DES+VHS + VIKING data. Among these, 76 184 objects have AllWISE W1 and W2 bands. The next step is to infer a photo-type for each object in the target sample.

4 PHOTO-TYPE CLASSIFICATION

To infer a spectral type for objects in the target sample, we also closely follow the procedure described by Carnero Rosell et al. (2019), originally from Skrzypek et al. (2015). The spectral type

Table 2. Updated template colours of M0–T9 dwarfs.

SpT	i–z	z–Y	Y–J	J–H	H–Ks	Ks–W1	W1–W2
M0	0.28	0.08	1.12	0.59	0.17	0.09	0.01
M1	0.35	0.10	1.14	0.57	0.20	0.12	0.05
M2	0.42	0.12	1.17	0.55	0.22	0.13	0.09
M3	0.50	0.14	1.20	0.53	0.23	0.15	0.13
M4	0.58	0.16	1.23	0.52	0.25	0.17	0.15
M5	0.67	0.19	1.27	0.51	0.27	0.18	0.18
M6	0.81	0.24	1.34	0.51	0.30	0.20	0.19
M7	0.98	0.30	1.42	0.52	0.34	0.22	0.20
M8	1.18	0.37	1.53	0.54	0.37	0.23	0.19
M9	1.37	0.44	1.63	0.57	0.42	0.26	0.23
L0	1.53	0.55	1.92	0.63	0.49	0.40	0.32
L1	1.53	0.54	2.05	0.63	0.52	0.41	0.31
L2	1.54	0.54	2.15	0.68	0.56	0.47	0.31
L3	1.56	0.55	2.23	0.76	0.60	0.56	0.32
L4	1.61	0.56	2.27	0.84	0.64	0.66	0.33
L5	1.68	0.58	2.30	0.92	0.66	0.74	0.35
L6	1.78	0.60	2.32	0.97	0.67	0.81	0.38
L7	1.92	0.63	2.32	0.99	0.65	0.85	0.43
L8	2.08	0.66	2.31	0.97	0.62	0.86	0.49
L9	2.26	0.69	2.30	0.91	0.57	0.83	0.57
T0	2.46	0.74	2.29	0.80	0.50	0.78	0.68
T1	2.68	0.78	2.29	0.66	0.42	0.70	0.81
T2	2.89	0.84	2.30	0.49	0.33	0.60	0.96
T3	3.09	0.90	2.32	0.30	0.24	0.51	1.15
T4	3.26	0.96	2.36	0.09	0.15	0.42	1.36
T5	3.39	1.03	2.42	−0.09	0.07	0.38	1.61
T6	3.46	1.10	2.51	−0.25	0.02	0.40	1.90
T7	3.45	1.18	2.62	−0.36	0.01	0.50	2.22
T8	3.33	1.26	2.78	−0.39	0.04	0.72	2.59
T9	3.08	1.35	2.97	−0.30	0.15	1.10	3.00

will be assigned by the minimization of the χ^2 relative to our new empirical templates presented in Table 2. Only objects that have measurements in a minimum of $N_{\text{bands}} = 6$ bands (thus yielding five colour indices) are considered as having a reliable photo-type. We applied this minimum of six bands because we have observed a substantial improvement in photo-type determination with the number of filters available. The χ^2 for the k-th source and the j-th spectral type is

$$\chi^2(\{m_b\}, \{\sigma_b\}, \hat{m}_{z,k,j}, \{c_b\}) = \sum_{b=1}^{N_{bands}} \left(\frac{m_{b,k} - \hat{m}_{z,k,j} - c_{b,j}}{\sigma_{b,k}} \right)^2$$

where $m_{b,k}$ are the measured magnitudes for the source in all available filters, and $c_{b,j}$ are the template colours for the j-th spectral type and for the same bands. These latter are measured for all templates with respect to a reference band (in our case, the z band). The $\sigma_{b,k}$ are the k-th source's photometric errors added in quadrature to the intrinsic scatter (from Section 3). As for $\hat{m}_{z,k,j}$ in equation 2.1, it is the inverse variance weighted estimate of the reference magnitude, computed using all the source's magnitudes, their associated uncertainties and the given template colours for the j-th type as follows:

$$\hat{m}_{z,k,j} = \frac{\sum_{b=1}^{N_{bands}} \frac{m_{b,k} - c_{b,j}}{\sigma_{b,k}^2}}{\sum_{b=1}^{N_{bands}} \frac{1}{\sigma_{b,k}^2}}.$$

4.1 Comparison with the literature

Fig. 3 shows the comparison between the spectral type from the literature and the photo-type method applied to the B2020 sample. As mentioned earlier, only objects with six or more valid magnitudes

are shown. Only one object has a misclassification bigger than four spectral types: ULAS J223347 + 002214. However, this object is known as a strong binary candidate (Day-Jones et al. 2013). The accuracy[1] for the B2020 sample is $\sigma_L = 1.7$ and $\sigma_T = 1.1$ for L and T dwarfs, respectively. These values can be considered as an upper limit to the uncertainty in the assigned type. These values are compatible with those obtained by Carnero Rosell et al. (2019) and Skrzypek et al. (2015). After testing the classification code, we obtain a photo-type for each object in our target sample. We used both DES+VHS+VIKING and DES+VHS+VIKING + AllWISE catalogues to estimate a photo-type. Our target sample now have 53 565 objects with photo-type ≥ L0 and six or more bands.

Besides B2020, we also expect to recover in our target sample other UCDs candidates from the literature that are located in the DES footprint. As explained before, the colour selection was made considering objects that have spectroscopic confirmation, but these are currently limited in number. We thus benefit from assessing our sample selection by cross-matching our candidates to other sizeable samples of candidate sources, not only because of the increased numbers but also because this allows a direct comparison of different photo-types.

From the 1361 objects presented by Skrzypek, Warren & Faherty (2016), 154 are located in the DES footprint and 78 of them are present in our target sample. The missing 76 sources are due to three main reasons: (i) a few objects are eliminated due to the colour selection and quality cuts applied to the DES data; (ii) some are eliminated due to separation beyond 2 arcsec match radius; (iii) the main reason, however, is that most of them are eliminated because of our demand on availability of VHS + VIKING data.

Reylé (2018) presented a sample of 14 915 ≥M7 and L candidates from the Gaia DR2 data, of which 2224 are located in the DES footprint. However, only 40 of them are L dwarfs candidates and the remaining objects are M dwarfs. We end up with 248 of their objects in our target sample, 20 of which are L candidates and the remaining are M dwarfs (78 M7/M7.5, 102 M8/M8.5, and 48 M9/M9.5). The missing 20 L dwarfs were eliminated by either one of the reasons we mention above. The reduced number of M dwarfs in our sample is due to the colour cuts imposed, as described in Section 3. Fig. 4 shows the comparison between the photo-types estimated from our classification code and those from these two other samples of UCD candidates. The median photo-type difference is of 0.5 for both Skrzypek et al. (2016) and Reylé (2018) for objects with $z <$ 19. For fainter magnitudes we can only compare to the Skrzypek et al. (2016) sample as Reylé (2018) is limited in $z < 19$ in our DES sample. For $19 < z < 21$ the median discrepancy is also 0.5.

5 TOWARDS THE FINAL SAMPLE: TARGET VALIDATION

5.1 Extragalactic contamination

As in Carnero Rosell et al. (2019), we removed possible extragalactic contamination by running the LEPHARE photo-z code (Arnouts et al. 1999; Ilbert et al. 2006) on the target sample using both a galaxy and quasar templates. We considered as extragalactic all sources that satisfied the following condition: $\chi^2_{\text{Lephare}} < \chi^2_{\text{classif}}$, where χ^2_{Lephare} and χ^2_{classif} are the best-fitting χ^2 values from LEPHARE and from our photo-type code, respectively.

---

[1] $\sigma = \frac{\sum_{j=1}^{N} |\Delta Sp.T|}{N} \frac{\sqrt{2\pi}}{2}$
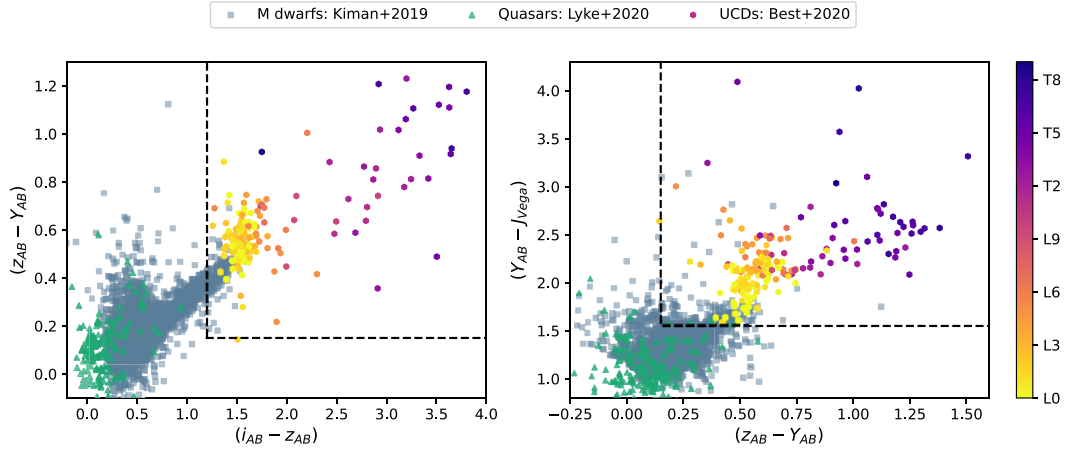
Figure 2. Colour–colour diagrams for the M dwarfs (Kiman et al. 2019; blue squares), L and T dwarfs (Best & et al. 2020), shown as circles, and quasars with z > 4 (Lyke et al. 2020; green triangles). The colour coded represents objects with spectral type L0 and later. The black lines indicate the colour selection.
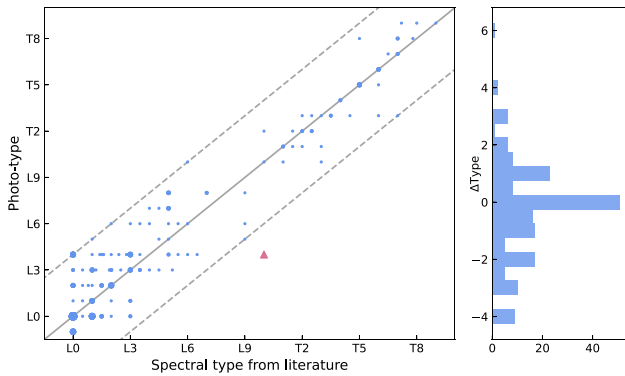

Figure 3. Spectral classification from B2020 compilation against our photo-type classification. The dashed lines represent misclassification by four spectral types. The size of the circles scales as the cube of the number of repeated points. The histogram on the right shows the differences between the spectral types from the literature and our photo-types (ΔType).

Figure 4. Photo-type classification from Skrzypek et al. (2016) and Reylé (2018; x-axis) and our photo-type classification (y-axis). The dashed lines represent misclassification by four spectral types. The histogram on the right shows the differences between the photo-types from the literature and our photo-types (ΔType).

From the 164 406 objects presented in our initial sample, only 53 565 have six or more bands and have a photo-type L0 and later. From this catalogue of 53 565 L and T candidates, 34 116 were flagged as an extragalatic sources by LEPHARE. Therefore, our final L and T dwarf candidate sample are constituted by a total of 19 449 objects. We also matched the 53 565 L and T dwarf candidates to SIMBAD (Wenger et al. 2000) astronomical database in order to verify if the results provided by LEPHARE were in agreement with the literature. We found 327 objects in common, using a matching radius of 2 arcsec. From this list, only 63 were extragalactic sources and LEPHARE was able to discard 56. The seven objects that remained in the sample were discarded. As discussed in Carnero Rosell et al. (2019), a residual contamination by extragalactic sources is estimated to be ∼ 5 per cent.

We also tested running LEPHARE in the B2020 sample to verify the effect of the code on a pure UCD sample and only one object was flagged as an extragalactic: ULAS J222711-004547. ULAS J222711-004547 is known in the literature as a peculiar L dwarf. Since one ultracool dwarf was flagged as extragalatic by LEPHARE we decided to further investigate the 34 116 sources that were flagged as extragalatic

sources using their proper motion information. In the next section we will discuss the details.

5.2 Proper motion

In addition to LEPHARE, we used available proper motion catalogues in order to assess the Galactic or extragalactic nature of our candidate L and T dwarfs. If the source has a proper motion significantly different from zero, it is likely a Galactic one. We decided to use the proper motions from Gaia DR3 (Gaia Collaboration 2022), the CatWISE2020 catalogue (Marocco et al. 2021), and the NOIRLab Source Catalog (NSC) DR2 (Nidever et al. 2021). In particular, these last two catalogues extend towards faint enough magnitudes to cover
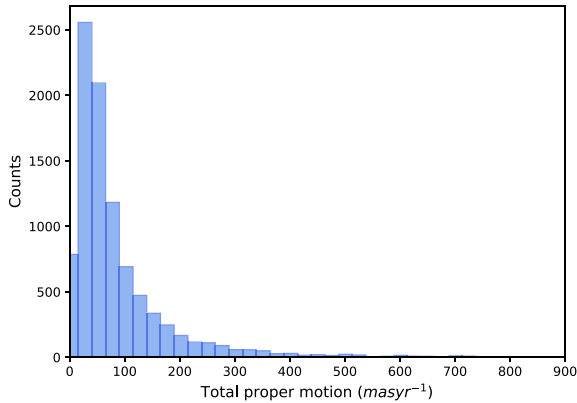
Figure 5. Distribution of total proper motions for ultracool dwarf candidates in our sample. We only show here objects with well-measured proper motion according to our criteria presented in Section 5.2.

Figure 6. Photo-type comparison between our new classification and the results from Carnero Rosell et al. (2019; ΔType). The histogram in the right shows that the vast majority of the objects have a difference of one spectral type, most now being classified as a slightly earlier type.

a significant fraction (96 per cent) of our target sample of 53 565. These catalogues are responsible for several new discoveries, such as extreme T/Y subdwarfs (Kirkpatrick et al. 2021b; Meisner et al. 2021), new ultracool dwarfs members of the Solar Neighbourhood (Kota et al. 2022), and new wide binary systems (Kiwy et al. 2022; Softich et al. 2022). It is important to mention that in our sample of 53 565 L and T candidates, only 320 sources have Gaia DR3 proper motion measurements (this includes objects with RUWE < 1.4 that ensures a good astrometric solution).

We apply $\sigma_\mu/\mu < 0.5$ for all catalogues as a criterion for them to be considered Galactic sources. In the case of NSC, for some objects with large proper motion errors, $\sigma_\mu > 1000$ mas yr^{-1}, we felt the need to apply a more stringent selection criterion, $\sigma_\mu/\mu < 0.1$. Considering objects with Gaia DR3 proper motion measurements, for instance, only 12 out of the 320 sources are classified as an extragalactic source by LEPHARE. However, 11 of them have proper motion from Gaia DR3 that satisfy our criteria. For the remaining objects flagged as extragalactic, 25 039 have proper motion measurements from CatWISE and NSC catalogues. In this case, 130 satisfies the criteria presented above. In total, 141 objects return to the L and T candidates sample. We conclude that proper motion data in conjunction with our adopted criteria do serve as a means to recover Galactic sources mistakenly classified as extragalactic by other means. Therefore, we have now 19 583 L and T dwarf candidates in the final sample. Fig. 5 shows the distribution of total proper motion ($\mu_{tot} = \sqrt{\mu_{\alpha cos\delta}^2 + \mu_\delta^2}$) for the objects that satisfy the condition $\sigma_\mu/\mu < 0.5$ at least in one catalogue (Gaia DR3, CatWISE2020, or NSC DR2). This sample has 9278 objects.

5.3 Comparison with our previous work

From the objects presented in Carnero Rosell et al. (2019), 10 440 L and T dwarfs are present in the initial 164 406 sample of this paper (see Table 1). The missing objects are due to a combination of slight changes in the DES footprint, the quality selection made in the target sample, changes in flags and photometric error criteria, and of lack of data in VHS + VIKING catalogues.

Imposing that the target must have six or more bands, something that was not applied in the past work, we end up with 8512 in common. However, 5342 objects are now classified as L or later. The remaining 3170 are now classified as M9. This large migration across the M9/L0 border is expected due to the larger intrinsic scatter
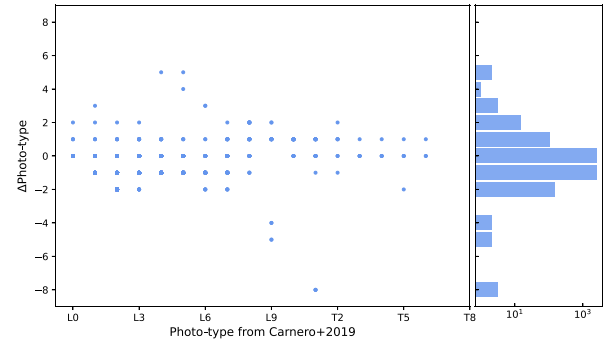
adopted here when compared to the previous work, as explained in Section 3. Besides, we used the GalmodBD simulation code (Carnero Rosell et al. 2019) to estimate the reverse effect, namely the contamination of M dwarfs to this new sample. We expect that ~ 30 per cent of our sample is made up of late M dwarfs, the vast majority of them of M9 type. This is again somewhat larger than the 15–20 per cent estimated in our previous work. We should emphasize, however, that that this contamination is from sources of a very similar nature to our target L dwarfs. From the 5342 L and T dwarfs still present on our sample, 24 were flagged as an extragalactic source either by LEPHARE or were listed in SIMBAD database. However, two flagged by LEPHARE have a proper motion measurement that satisfied our criteria. Therefore, in the end, 5320 original L and T dwarfs from Carnero Rosell et al. (2019) remain in the new sample presented here, while most of the missing ones are now classified as late M type. Fig. 6 shows the comparison between the photo-types from the previous work and those of the new candidate sample for objects in common.

5.4 New ultracool dwarf candidates

In total, 19 583 objects remain in our candidate sample, following all the criteria presented earlier. However, from this sample, 142 are included B2020, 5257 additional ones were presented in Carnero Rosell et al. (2019), 26 from Reylé (2018), 5 from Skrzypek et al. (2016), and 54 from SIMBAD (mostly late-M dwarfs from other references, hence surveys, than those used here). There are 14 099 new UCD candidates. The table containing the ultracool dwarf candidates is available at https://des.ncsa.illinois.edu/releases/other/Y6-LTdwarfs.

Fig. 7 shows the photo-type distribution vs photometric distance of the candidate sample of UCDs from this work. The final sample has only objects with six or more bands (used to estimate the photo-type), $\chi^2_{classif} < \chi^2_{Lephare}$ (or otherwise total proper motion significantly different from zero, if available) and a photo-type $\geq$L0. Here we see that this new sample is probing larger distances than those presented in Carnero Rosell et al. (2019). We now reach over 600 pc, while in our previous work we reached ~ 480 pc.

We estimate photometric distances for our candidates following the same procedure explained in Carnero Rosell et al. (2019). We first calculate the absolute magnitudes for the UCD templates discussed in the previous chapter for all photometric bands and spectral types. We do that by using the template colours shown in Table 2 and anchoring the absolute magnitude scale to the M_{W2} values presented by Dupuy &
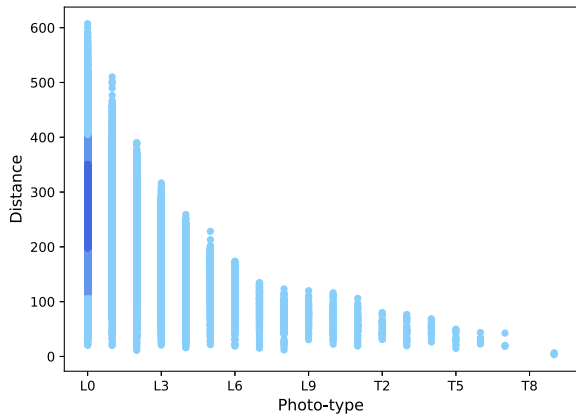
Figure 7. Distances as a function of photo-type. Distances have been calculated using the average value from the distance modulus obtained using all available bands. The colour scale represents the density. Most ultracool dwarf candidates are early L at distances smaller than 650 pc.
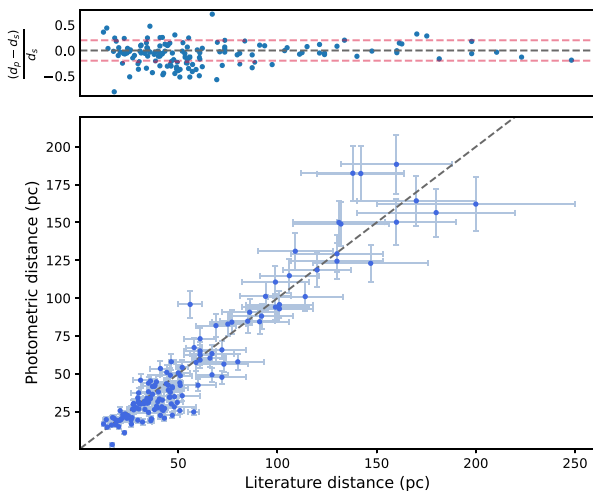

Figure 8. Comparison between our photometric distances (d_p) and distances from the B2020 compilation (d_s), which has a mixture of trigonometric parallaxes and photometric distances. Our photometric distances tend to be slightly underestimated compared to those presented in B2020.

Liu (2012). The distance for each UCD candidate in our sample is then determined from all its available apparent magnitudes and the template absolute magnitudes corresponding to its assigned spectral type. The mean distance over all available bands is assigned as the UCD distance. The distance uncertainty is obtained considering the photometric errors added in quadrature with the intrinsic scatter for each available band. We did not apply any correction for extinction, since this is expected to be small for the passbands we used and towards the relatively high Galactic latitudes covered by our sample.

We checked our photometric distances comparing with those presented in B2020, which comprehends several parallax and photometric measurements from the literature, as shown in Fig. 8. Our photometric distances tend to be slightly underestimated relative to those from B2020. This effect results from a tendency of assigning later types for the objects. Comparing our distance estimates and those from B2020 that have trigonometric parallax distances, the typical error in our photometric distances is ~28 per cent. Also, the systematic offset seen in the figure, in the sense of our distances

being underestimated, is 18 per cent when we considered all objects from B2020, independent of the distance measurement method.

6 UCD CANDIDATES CATALOGUE APPLICATIONS

6.1 Young moving groups and association candidates

Young moving groups and associations contain young stars ($\sim$ 10–100 Myr) and substellar objects whose similar kinematics imply that they originated in the same star-forming region. The members of a young association are a coeval population, where stars can serve as benchmarks to constrain metallicities and ages for substellar objects and to study models of star formation, for instance. Since our search targeted the general ultracool dwarfs population, we used the BANYAN Σ code (Gagné et al. 2018) to estimate if any object in our sample is likely a moving group candidate member. The BANYAN Σ algorithm uses a compiled list of bonafide members of 29 YMGs and associations within 150 pc of the Sun and field stars within 300 pc to compute membership probability given the sky position, proper motion, distance, and radial velocity of targets using Bayesian inference. In our analyses, we divided the sample into: (i) targets with Gaia DR3 information; (ii) targets with CatWISE or NSC proper motion. For these latter, we also demanded that $\sigma_\mu/\mu < 0.5$. Also, we added in the samples radial velocity measurements from the literature when available.

It is important to mention that we ran BANYAN Σ twice if the object has CatWISE2020 and NSC DR2 proper motion. In this case, we only kept candidates whose BANYAN results were the same. We found that 60 objects among our list were already reported in the literature as moving groups candidate members. The recovered members are shown in Table 3 and Table 4 along with new candidates. Table 3 contains only the objects with proper motion and parallax from Gaia DR3. Table 4 contains objects with proper motion from CatWISE2020 and NSC DR2, photometric distances, and BANYAN Σ probabilities according to the catalogue used. We also added in both tables the spectral type from the literature (when available) besides our photo-type. The objects from the literature have added to their spectral type the gravity subtypes α, β, and γ to designate objects of normal gravity, intermediate gravity, and very low gravity, respectively. Also, the δ suffix denotes objects with an even younger age (typically less than a few Myr) and lower surface gravity than those associated with the γ suffix (Kirkpatrick et al. 2006).

The YMGs candidates (new and recovered) that we found are: 20 in AB Doradus (AB Dor, 110–150 Myr; Luhman, Stauffer & Mamajek 2005; Barenfeld et al. 2013), six in β Pictoris (β Pic, 22 ± 6 Myr; Shkolnik et al. 2017), 11 in Columba (Col, 42^{+6}_{-4} Myr; Bell, Mamajek & Naylor 2015), one in Carina (Car, 45^{+11}_{-7} Myr; Bell et al. 2015), three in Carina-Near (CarN, 200 ± 50 Myr; Zuckerman et al. 2006), one in Octans (OCT, 35 ± 5 Myr; Murphy & Lawson 2015), and 25 in Tucana-Horologium (THA, 45 ± 4 Myr; Bell et al. 2015). We did not include any candidate member from Argus association considering its high level of contamination (Bell et al. 2015).

We found 20 new candidate members to young associations with Bayesian membership probability above 90 per cent, at least in one catalogue. For objects in common with the literature, we analysed each case individually considering not only the difference in kinematics between this work and previous ones (our work probably making use of more recent and robust proper motion measurements), but also the use of BANYAN Σ (more recent and updated code) results in substitution to those presented by BANYAN II or BANYAN

Table 3. Ultracool dwarfs new candidates and members recovered from the literature of YMGs and associations.

Object Name	RA deg	DEC deg	Ph.T	SpT	$\mu_\alpha \cos\delta$ mas yr^{-1}	μ_δ mas yr^{-1}	Parallax mas	RV km s^{-1}	Prob.	Ref.
AB Doradus										
Recovered previously candidate members										
J003256-440507	8.2335	−44.0854	L3	L0 γ	127.84 ± 0.28	−96.83 ± 0.31	28.95 ± 0.42	-	99 per cent	2,3,5,6
J013847-345232	24.6981	−34.8756	L0	-	74.99 ± 0.47	−52.01 ± 0.38	18.76 ± 0.63	-	93 per cent	3
J031645-284853	49.1886	−28.8149	L2	L0	103.90 ± 0.22	−94.71 ± 0.30	30.23 ± 0.34	-	98 per cent	1,2,7
J032529-431230	51.3728	−43.2084		M9	66.79 ± 0.26	−20.77 ± 0.30	18.49 ± 0.25	-	88 per cent	1
J043350-421241	68.4578	−42.2114		M9∗	57.23 ± 0.26	−29.37 ± 0.29	22.92 ± 0.24	-	93 per cent	3
J220645-421723	331.6883	−42.2900	L6		128.67 ± 0.90	−184.88 ± 0.93	34.08 ± 1.30	-	99 per cent	1,2,7
β Pictoris										
Recovered previously candidate members										
J045327-175155	73.3605	−17.8652	L3	L3	44.39 ± 0.38	−20.60 ± 0.39	33.06 ± 0.54	-	99 per cent	1,7,8
Carina										
Recovered previously candidate members										
J043531-644956	68.8773	−64.8323	L1	M8.5	49.55 ± 1.33	36.32 ± 0.89	18.49 ± 0.61	19.7 ± 1.0	99 per cent	1,7
Carina-Near										
Recovered previously candidate members										
J051929-450638	79.8699	−45.1106	L0	L2∗	39.43 ± 0.91	66.55 ± 1.20	18.47 ± 0.98	-	96 per cent	3
Columba										
New candidate members										
J051007-530626	77.5307	−53.1072	L0	-	26.57 ± 0.95	20.62 ± 1.31	11.18 ± 0.83	-	90 per cent	
Recovered previously candidate members										
J003443-410228	8.6798	−41.0410	L4	L1 β	107.91 ± 0.80	−59.28 ± 1.56	21.54 ± 1.18	-	82 per cent	1,2,7
J050816-455751	77.0682	−45.9641	L0	M8∗	25.33 ± 0.49	13.94 ± 0.64	11.64 ± 0.45	-	99 per cent	3
J051846-275646	79.6925	−27.9460	L4	L1 γ	33.84 ± 0.51	−4.82 ± 0.60	18.28 ± 0.59	24.35 ± 0.19	99 per cent	2,5,6,7
J055048-302006	87.6999	−30.3351	L1	M9.4	20.46 ± 0.67	−0.59 ± 0.85	18.50 ± 0.74	23.9 ± 1.4	99 per cent	1,6
J055538-413349	88.9064	−41.5635	L2	L0.4	22.65 ± 0.83	15.76 ± 0.80	18.54 ± 0.65	23.5 ± 1.5	99 per cent	1,6
Tucana-Horologium Association										
Recovered previously candidate members										
J000658-643655	1.7423	−64.6154	L0		86.20 ± 0.19	−61.60 ± 0.21	23.17 ± 0.19	-	99 per cent	1,6
J003743-584624	9.4301	−58.7732	L4	L0 γ	86.99 ± 0.91	−49.95 ± 1.05	20.64 ± 0.81	6.62 ± 0.07	99 per cent	2,4,6,7
J003815-640354	9.5629	−64.0649	L1	M9.5 β	86.51 ± 0.30	−47.71 ± 0.29	21.75 ± 0.27	-	99 per cent	2
J011748-340327	19.4485	−34.0574	L3	L1 β	108.27 ± 0.58	−58.06 ± 0.71	25.40 ± 0.70	-	99 per cent	2,4,6
J012051-520036	20.2139	−52.0099	L4	L1 γ	101.59 ± 0.89	−44.85 ± 1.17	24.26 ± 0.94	-	99 per cent	1,6,7
J014158-463358	25.4934	−46.5661	L4	L0 γ	116.73 ± 0.35	−46.62 ± 0.48	27.29 ± 0.44	6.41 ± 1.56	99 per cent	6,7
J021039-301532	32.6612	−30.2589	L2	L0 γ	101.63 ± 0.55	−44.09 ± 0.51	24.65 ± 0.48	7.82 ± 0.27	99 per cent	2,6,7
J022155-541206	35.4799	−54.2016	L0	M9 β	110.74 ± 0.20	−21.91 ± 0.20	26.46 ± 0.19	10.18 ± 0.1	99 per cent	2,4,6,7
J022355-581507	35.9786	−58.2519	L4	L0 γ	105.22 ± 0.51	−16.44 ± 0.50	25.17 ± 0.44	10.36 ± 0.23	99 per cent	2,4,6,7
J022520-583730	36.3320	−58.6250	L0	M9 β	100.88 ± 0.20	−14.97 ± 0.20	24.25 ± 0.17	10.7 ± 2.2	99 per cent	2,4,6,7
J022657-532703	36.7365	−53.4510	L3	L0 δ	92.44 ± 0.47	−18.78 ± 0.59	21.76 ± 0.43	-	99 per cent	1,6,7
J023401-644207	38.5049	−64.7020	L2	L0 γ	87.82 ± 0.65	−4.93 ± 0.75	20.81 ± 0.62	11.76 ± 0.72	99 per cent	2,4,5,6,7
J024012-530553	40.0511	−53.0980	L0	M9.5	96.30 ± 0.24	−14.22 ± 0.28	23.49 ± 0.24	10.9 ± 2.2	99 per cent	6,7
J024106-551147	40.2743	−55.1963	L4	L1 γ	99.14 ± 0.86	−13.3 ± 1.15	23.86 ± 0.80	11.73 ± 2.44	99 per cent	1,7
J024351-543220	40.9634	−54.5388	L0	M9	91.71 ± 0.21	−11.24 ± 0.22	22.29 ± 0.20	11.2 ± 2.2	99 per cent	6,7
J030149-590302	45.4545	−59.0506	L0	M9	81.33 ± 0.17	−2.01 ± 0.19	19.88 ± 0.15	12.3 ± 2.2	99 per cent	6,7
J031143-323945	47.9273	−32.6626	L1	M9.8∗	94.97 ± 0.43	−24.90 ± 0.47	25.63 ± 0.56	10.6 ± 2.2	66 per cent	1
J032310-463124	50.7922	−46.5232	L4	L0 γ	85.55 ± 0.87	−7.32 ± 0.89	23.41 ± 0.70	13.0 ± 0.05	99 per cent	2,5,6,7
J035727-441731	59.3628	−44.2918	L2	L0 β	76.69 ± 0.30	−0.97 ± 0.41	21.28 ± 0.29	10.73 ± 4.6	99 per cent	2,5,6,7
J044010-512654	70.0409	−51.4484	L3	L0 γ	55.98 ± 1.23	18.87 ± 1.94	19.08 ± 1.15	15.6 ± 2.1	99 per cent	1,6
J045521-544616	73.8380	−54.7710	L0	M9∗	54.09 ± 0.40	23.20 ± 0.45	19.09 ± 0.32	-	99 per cent	3
J223536-590632	338.8989	−59.1089	L0	M8.5	60.36 ± 0.20	−84.16 ± 0.22	21.33 ± 0.23	2.9 ± 2.2	99 per cent	2,6,7
J232253-615129	350.7216	−61.8580	L4	L2	79.29 ± 0.80	−80.17 ± 1.09	23.33 ± 0.96	6.75 ± 0.75	99 per cent	1,5,6,7

Note. The objects in this table have proper motion and parallax from Gaia DR3 catalogue. **References:** (1) Gagné et al. (2015); (2) Faherty et al. (2016); (3) Gagné et al. (2018); (4) Naud et al. (2017); (5) Vos et al. (2019); (6) Riedel et al. (2017); (7) Ujjwal et al. (2020).
∗Photo-Type estimated using photometry.

I, for instance. 12 objects are now classified as field members according to our results and are not presented in the following tables. The ambiguous objects were placed in the group indicated by our BANYAN Σ run. The objects with discrepancies in the classification are:

(i) *J003443-410228*: this object was first presented in Faherty et al. (2016) and more recently in Ujjwal et al. (2020) as a THA candidate member. However, using proper motion and parallax measurements from Gaia DR3, we identified it as Col candidate member (83 per cent of probability).

Table 4. Moving groups candidates with CatWISE2020 and NSC DR2 proper motion information.

Object	RA	DEC	Ph.T	SpT	$\mu_\alpha \cos\delta$	μ_δ	$\mu_\alpha \cos\delta$	μ_δ	Distance	RV	Prob.
AB Doradus											
New candidate members											
J020047-510522	30.1975	−51.0894	L8	-	167.11 ± 4.40	−85.81 ± 3.9	175.52 ± 2.28	−68.00 ± 2.33	22.34 ± 2.06	-	99–99 per cent
J022609-161001	36.5383	−16.1669	L8	-	103.18 ± 6.40	−106.56 ± 5.70	109.59 ± 7.99	−128.34 ± 8.22	31.50 ± 2.92	-	98–99 per cent
J023618 + 004852	39.0753	0.8144	L4	-	124.50 ± 7.10	−161.35 ± 6.50	134.52 ± 2.61	−168.00 ± 2.92	37.39 ± 3.45	-	92–75 per cent
J040232-264020	60.6320	−26.6722	T1	-	65.09 ± 24.00	−59.59 ± 25.60	80.81 ± 10.08	−66.82 ± 10.00	46.43 ± 4.40	-	90–81 per cent
J043250-562131	68.2098	−56.3587	L4	-	29.30 ± 7.70	24.86 ± 6.40	33.48 ± 2.22	19.43 ± 2.18	55.04 ± 5.09	-	85–95 per cent
J044842-592802	72.1762	−59.4673	L7	-	22.38 ± 8.60	19.56 ± 7.20	27.27 ± 5.30	12.99 ± 5.30	53.13 ± 4.94	-	94–95 per cent
J050656-251439	76.7333	−25.2442	L8	-	38.45 ± 8.30	−61.19 ± 8.30	36.50 ± 12.26	−64.88 ± 12.25	41.29 ± 3.84	-	98–98 per cent
J050928-311207	77.3671	−31.2018	L5	-	29.91 ± 10.00	−41.56 ± 9.50	25.01 ± 5.77	−32.87 ± 5.87	50.23 ± 4.65	-	96–97 per cent
J051244-502007	78.1825	−50.3351	L4	-	43.30 ± 5.40	14.75 ± 4.90	43.73 ± 2.47	19.18 ± 2.39	35.33 ± 3.26	-	99–98 per cent
J052114-373332	80.3095	−37.5590	L5	-	10.21 ± 7.20	−35.93 ± 7.19	15.46 ± 2.46	−40.04 ± 2.52	35.79 ± 3.31	-	98–99 per cent
J053808-493406	84.5327	−49.5683	L2	-	26.25 ± 7.60	1.05 ± 7.30	13.32 ± 1.86	−2.46 ± 1.88	58.22 ± 5.38	-	81–94 per cent
Recovered previously candidate members											
J032642-210208	51.6765	−21.0356	L8	L5 β	83.09 ± 5.00	−143.70 ± 4.50	90.57 ± 3.42	−144.60 ± 3.13	19.48 ± 1.80	22.91 ± 20.07	65–89 per cent
J040627-381210	61.6117	−38.2028	L4	L0 γ	37.72 ± 7.90	−11.14 ± 7.50	41.90 ± 5.38	1.90 ± 5.53	47.70 ± 4.41	-	66 per cent
J041352-401009	63.4646	−40.1692	L4	L2.5	53.82 ± 7.9	−10.1 ± 7.1	39.45 ± 3.17	4.22 ± 3.19	47.56 ± 4.39	-	76 per cent
β Pictoris											
New candidate members											
J045544-250107	73.9353	−25.0187	L5	-	43.48 ± 8.20	−0.22 ± 8.00	31.09 ± 4.78	−9.96 ± 4.95	41.72 ± 3.86	-	89–98 per cent
J202436-544944	306.1502	−54.8289	L8	-	37.74 ± 10.60	−86.00 ± 9.90	53.44 ± 11.51	−82.63 ± 11.65	42.28 ± 3.94	-	88–98 per cent
J213422-582853	323.5926	−58.4814	L8	-	61.87 ± 14.10	−93.82 ± 13.00	85.69 ± 5.11	−88.91 ± 5.22	43.14 ± 4.01	-	62–92 per cent
Recovered previously candidate members											
J034209-290432	55.5391	−29.0755	L3	L0 β	37.26 ± 7.2	0.44 ± 6.6	60.95 ± 2.78	−7.79 ± 2.90	42.31 ± 3.91	-	93 per cent
J053620-192040	84.0834	−19.3445	L6	L2 γ	31.73 ± 5.50	−13.04 ± 5.60	33.24 ± 2.48	−18.65 ± 2.54	22.58 ± 2.08	22.06 ± 0.70	99–98 per cent
Carina-Near											
New candidate members											
J033555-443916	53.9784	−44.6545	T5	-	161.37 ± 17.90	133.76 ± 17.60	209.40 ± 6.07	125.57 ± 5.88	27.03 ± 2.59	-	86–95 per cent
J042013-253924	65.0526	−25.6567	L6	-	90.09 ± 9.30	71.09 ± 9.20	95.23 ± 4.99	63.46 ± 4.85	42.72 ± 4.82	-	79–92 per cent
Columba											
New candidate members											
J043838-460256	69.6573	−46.0488	L5	-	38.75 ± 8.20	7.94 ± 7.60	39.61 ± 2.85	14.01 ± 2.88	48.05 ± 4.44	-	67–94 per cent
Recovered previously candidate members											
J031819-643322	49.5772	−64.5561	L2	-	48.75 ± 7.80	9.05 ± 7.00	48.62 ± 2.32	8.18 ± 2.28	59.03 ± 5.46	12.6 ± 2.4	54 per cent
J041859-450741	64.7453	−45.1281	L4	L3 γ	60.44 ± 5.90	15.26 ± 5.00	58.56 ± 2.65	8.00 ± 2.51	38.00 ± 3.51	15.1 ± 2.1	83–92 per cent
J051050-184356	77.7070	−18.7321	L3	L2 β	81.77 ± 5.80	−50.12 ± 6.1	83 ± 3.01	−44.10 ± 2.98	31.86 ± 2.94	23.2 ± 1.3	97–55 per cent
J054008-364218	85.0345	−36.7050	L4	L2.3	21.47 ± 6.9	−3.23 ± 6.8	29.45 ± 2.52	4.49 ± 2.56	38.17 ± 3.53	-	99 per cent
Octans											
New candidate members											
J005503-533413	13.7636	−53.5703	L0	-	31.60 ± 9.30	28.61 ± 8.40	29.23 ± 1.58	16.56 ± 1.67	77.06 ± 7.13	-	96–71 per cent
Tucana-Horologium Association											
New candidate members											
J024725-492032	41.8555	−49.3423	L8	-	109.25 ± 7.60	−16.97 ± 6.60	106.75 ± 10.08	−28.82 ± 10.09	50.02 ± 4.71	-	92–80 per cent
Recovered previously candidate members											
J203345-563535	308.4365	−56.5931	L3	L0 γ	−3.95 ± 6.7	−74.19 ± 6.6	13.69 ± 2.47	−84.69 ± 2.72	40.66 ± 43.77	-	56 per cent

References: (1) Gagné et al. (2015); (2) Faherty et al. (2016); (3) Naud et al. (2017); (4) Vos et al. (2019); (5) Riedel et al. (2017); (6) Ujjwal et al. (2020). Candidates both new and recovered from the literature are listed.

(ii) *J031645-284853*: Faherty et al. (2016) presented as ambiguous AB Dor member by BANYAN II. More recently, Ujjwal et al. (2020) classified as THA candidate member. Here using Gaia DR3 proper motion and parallax we classified as AB Dor candidate member (98 per cent of probability).

(iii) *J040627-381210*: Riedel et al. (2017) classified this object as field member using the LACEwING code. However, Faherty et al. (2016) presented as Col candidate member using BANYAN II, Octans by LACEwING and field object by BANYAN I. Here, the use of NSC proper motion into BANYAN Σ also indicated as field object (66 per cent probability).

(iv) *J041352-401009*: Gagné et al. (2015) classified this object as Col candidate member. The BANYAN Σ classified as β Pic member when we used the NSC DR2 proper motion (32 per cent probability) and as AB Dor member using CatWISE2020 data (76 per cent of probability).

(v) *J034209-290432*: Gagné et al. (2015) and Riedel et al. (2017) classified this object as THA candidate member. Here, BANYAN Σ classified as field member when we used the CatWISE proper motion (94 per cent probability) and as a β Pic using NSC DR2 (93 per cent probability).

(vi) *J041859-450741*: Faherty et al. (2016) presented as ambiguous THA member by BANYAN II and AB Dor candidate by LACEwING and BANYAN I. Both Vos et al. (2019) and Riedel et al. (2017) identified this object as AB Dor candidate member. Here, BANYAN Σ identified as Col candidate member.

(vii) *J031819-643322*: Gagné et al. (2015) presented this object as THA member. Here, BANYAN Σ classified as field using NSC proper motion (99 per cent probability) and Col member using CatWISE2020 (53 per cent probability).

(viii) *J054008-364218*: Gagné et al. (2015) classified this object as Col candidate member. Here, BANYAN Σ classified as β Pic member when we used the CatWISE2020 proper motion (76 per cent probability) and as Col member using NSC DR2 data (99 per cent probability).
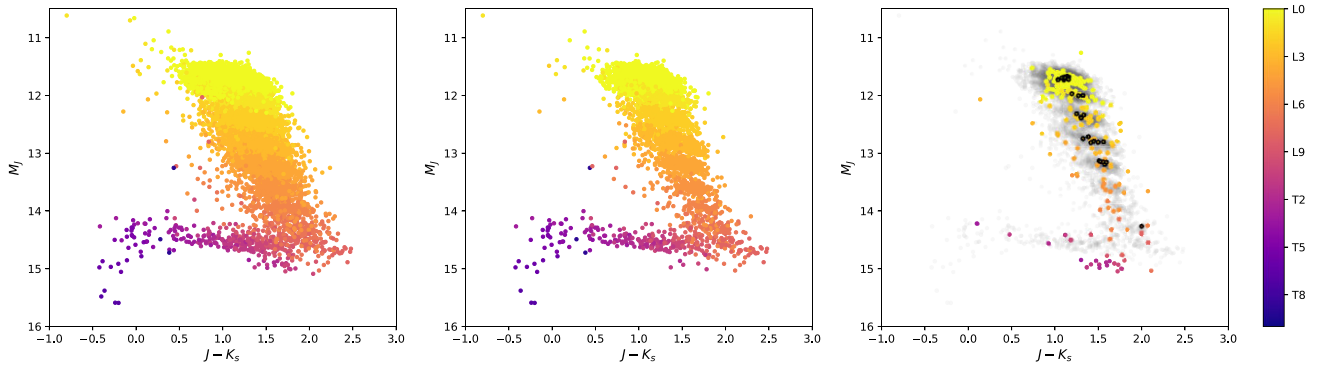
Figure 9. Colour J–K_s vs absolute magnitude in J band. The left-hand panel shows all the 19 583 ultracool dwarf candidates. The mid panel shows only ultracool dwarfs candidates with significant proper motion. The right-hand panel shows the photometric variable objects identified in the Dark Energy Survey Y6 variability catalogue. The points with black contour represent the 28 young candidate objects among the variable sample. The shaded background is made up of all sources from the middle panel.

(ix) *J203345-563535*: Gagné et al. (2015), Faherty et al. (2016), and Riedel et al. (2017) presented this object as THA member. Here BANYAN Σ classified as field member when we used the CatWISE2020 proper motion (99 per cent probability).

Despite the recovered and new candidate members to younger populations, still the vast majority of 99.1 per cent of our sample that has significant proper motion is composed of field objects. Also, it is important to mention that the comparison between our photo-type estimate and spectral type from candidate members of young associations from the literature shows a systematic discrepancy of up to $+4$ types in some cases. This may be the effect of deviant colours attributed to enhanced dust or thick photospheric clouds, that shift the flux to longer wavelengths in young objects (Faherty et al. 2016).

6.2 Variability

Photometric variability can help to understand atmospheric inhomogeneities in ultracool dwarfs, as it is sensitive to the spatial distribution of condensates as the object rotates. It has been studied in the more massive field L and T dwarfs, but still the variability of the younger and low-gravity objects is less understood. For instance, only a small sample of variability in low-gravity objects (Metchev et al. 2015; Vos et al. 2019) has been detected so far.

Here, we first used DES Y6 variability catalogue described in Stringer et al. (2021) to search for variable sources among our 19 583 ultracool candidates sample and we found 291 of those. There are several available statistics to select variable sources in this particular catalogue. The reduced χ^2 (RED_CHISQ_PSF_grizy ≥ 3.3) seems the most efficient to separate variable objects, for instance RR Lyrae, from standard stars. From these 291 variable candidate sources, 130 are also in the Transiting Exoplanet Survey Satellite (TESS) Input Catalog (Stassun et al. 2018), 28 are young objects already identified in the literature and that were discussed in the previous section and are presented in Tables 3 and 4. It is out of the purpose of this work to further analyse in detail these variable candidates. However, this type of sample may be a starting point for studies regarding the cloud formation and dissipation on brown dwarf atmospheres and to assess if low-gravity objects are more likely variable than their field ultracool dwarfs counterparts (Metchev et al. 2015).

Fig. 9 shows colour–magnitude diagrams for the entire sample of ultracool dwarf candidates presented in Section 5 (left-hand panel), for ultracool dwarf candidates that have significant proper motion (satisfy the criteria from Section 5.2; middle panel), and for the photometrically variable candidates identified in the DES variability catalogue (right-hand panel). From these latter, the 28 young candidate objects mentioned above are highlighted. Absolute magnitudes were calculated using our photometric distance estimates. The variable sources seem to roughly follow the same colour–magnitude properties as our full sample of ultracool dwarfs. We may not see subtle redder colours for the highlighted young L types because according to our methodology we tend to attribute later spectral types for young objects, as mentioned in the previous section. Here, 10 per cent of the young (L0–L7) candidate members to moving groups show photometric variability, a lower fraction when compared to Vos et al. (2019) that found $30 ^{+16}_{-8}$ per cent for the frequency of variable young objects in L0–L8.5 spectral type range. The remaining variable objects span the L0-T3 range of photo-types. We find that they correspond to 1.3 per cent of the total populations in the range L0–L8, and 7 per cent in the range L9–T3. These numbers are qualitatively similar to Radigan (2014), who found a higher variability of $24 ^{+11}_{-3}$ per cent for the L9-T3.5 range as compared to $3.2 ^{+2.8}_{-1.8}$ per cent outside the L/T transition.

6.3 Wide binary candidate systems

We also search for binary systems constituted by two ultracool dwarfs (L+L,L+T,T + T). This type of system is very interesting, since widely separated ultracool dwarf binaries are quite rare, especially considering field ages. A large number of wide binary systems in the Galactic field could in fact rule out formation scenarios where very low-mass and substellar objects are ejected from the protocluster due to dynamical interactions (Reipurth & Clarke 2001; Bate & Bonnell 2005). Due to their low binding energy, they are unlikely to survive this dynamical process.

A search for this type of binary system was previously presented in dal Ponte et al. (2020) using the sample of UCDs selected with the first DES data release. Here we used the same methodology and presented a new and updated list of this type of system. We used our UCD candidates catalogue to search for binaries, where we computed a search radius for each UCD and checked if another ultracool dwarf appears inside this individual radius. The search radius was defined as a projected separation of 10 000 AU evaluated at the lower limit in distance of the UCD.

Table 5. The common proper motion and distance pair candidates identified among the UCD sample.

ID	α_A	δ_A	α_B	δ_B	A	B	$\mu_\alpha \cos\delta$	μ_δ	$\mu_\alpha \cos\delta$	μ_δ	d_A	d_B	Sep (arcsec)	Ref.	Flag
		Position (deg)			Ph.T		Proper motion (mas yr^{-1})				Distance (pc)				
New Candidate Systems															
J004316-320343	10.815	−32.062	10.800	−32.110	T2	L9	−11.17 ± 18.00	46.72 ± 17.00	−19.65 ± 14.20	51.60 ± 13.80	41.86 ± 3.93	41.34 ± 3.85	176.5	5	101
J020903-124420	32.262	−12.739	32.262	−12.738	L0	L0	2.45 ± 4.78	22.89 ± 5.15	0.69 ± 4.92	33.54 ± 5.33	155.46 ± 14.81	151.94 ± 14.45	54.2	5	110
J022636-013744	36.651	−1.629	36.651	−1.629	L0	L0	6.05 ± 4.04	−38.40 ± 4.04	0.79 ± 4.01	−37.45 ± 4.01	166.28 ± 16.12	168.59 ± 16.37	2.4	5	110
J030422-135839	46.090	−13.977	46.049	−14.016	L6	L8	109.39 ± 13.8	45.14 ± 13.4	132.71 ± 36.1	32.35 ± 37.9	55.30 ± 5.15	90.09 ± 9.53	199.4	5	000
Recovered systems															
J013036-444542	22.648	−44.761	22.649	−44.761	L8	L0	124.98 ± 3.84	−33.63 ± 4.83	116.31 ± 1.44	−27.87 ± 1.74	27.00 ± 2.50	27.84 ± 2.57	3.1	2	110
J014611-050851	26.547	−5.147	26.546	−5.147	L4	L7	81.78 ± 1.98	−218.51 ± 1.93	80.51 ± 4.84	−214.01 ± 4.75	29.51 ± 2.73	45.07 ± 4.18	3.2	3	110
J055146-443411∗	87.941	−44.569	87.941	−44.570	L0	L0	−61.01 ± 1.38	−16.71 ± 1.44	−61.02 ± 0.88	−13.07 ± 0.83	76.64 ± 7.08	66.20 ± 6.12	2.2	1	111
J231349-455025	348.455	−45.840	348.455	−45.841	L5	L4	53.76 ± 12.33	6.06 ± 12.36	55.02 ± 4.94	13.36 ± 5.0	106.25 ± 10.25	81.25 ± 7.62	4.1	4	000

References: (1) Billères et al. (2005); (2) Dhital et al. (2011) (3) Softich et al. (2022); (4) dal Ponte et al. (2020); (5) This work.
∗Proper motion from Gaia DR3. The ID in *Jhhmm ± ddmm* format is based on the primary coordinates and the letters A and B represent a different UCD. The flag indicates 0 = common distance and common PM, the latest based on all available catalogues, 0 = common distance and common proper motion according to CatWISE2020, and 0 = common distance and common proper motion according to NSC DR2.

For the initial list of candidates, we required that $\Delta_\mu \leq 2\sigma_\mu$ where Δ_μ is the total proper motion difference,

$$\Delta_\mu = \sqrt{\Delta^2_{\mu_{\alpha\cos\delta}} + \Delta^2_{\mu_\delta}}$$

and $\Delta_{\mu_{\alpha\cos\delta}}$ and Δ_{μ_δ} are the differences in proper motion between the pair members. In the above criterion,

$$\sigma_\mu = \sqrt{\delta\mu_1^2 + \delta\mu_2^2}$$

is the composite uncertainty in the measured proper motions, where 1,2 represent different objects of the system. We again required that each object has $\sigma_\mu/\mu < 0.5$. The next step was to demand common distances, using a criterion at the 3σ level. The final list has four new candidates and four already known, both with common proper motion and distance. Of these, we note that only one system (J030422-135839) has a common distance beyond 2σ, which was the criterion adopted in dal Ponte et al. (2020). However, this system has proper motions that are in clear agreement with each other. Table 5 shows the new systems and those recovered from the literature. It is important to mention that not all systems presented in dal Ponte et al. (2020) were recovered here. The main reason is that some objects are now classified as M8 or M9 and therefore are not in the sample used for this new search.

To obtain the chance alignment probability we used the GalmodBD simulation code, which computes expected Galactic counts of ultra-cool dwarfs as a function of magnitude, colour, and direction on the sky. The code also creates synthetic samples based on the expected number counts for a given footprint, using empirically determined space densities of objects, absolute magnitudes and colours as a function of spectral type. We computed the expected number of UCDs in a given direction and within the volume bracketed by the common range of distances and by the area within the angular separation of each system. For all the four new binary candidates, the probability of chance alignment is < 0.004 per cent.

7 SPECTROSCOPIC CONFIRMATION OF 12 ULTRACOOL DWARFS

We undertook a spectroscopic project to further assess our UCDs search and classification methods. We got ~22 h of Gemini/GMOS time to obtain spectra for a small fraction of our UCD candidates, 12 objects in total. The target sample for the spectrocopic follow up was taken from dal Ponte et al. (2020). We have selected candidates that are more probable to be wide binary systems and for which the technical design will give us the best success rate. We also demanded the pair members to have a difference in distance modulus that was within 1.5 (1.0) from the typical expected difference given their

uncertainties. Finally, we avoided the largest physical separation pairs to reach the final target sample. Our targets have magnitudes within the range $19 < z_{DES} < 21.5$ and the preference was given for the systems composed by two L dwarfs. The purpose of this follow up spectroscopy was to confirm their nature, i.e. confront spectral type with our photo-type method and also to re-calculate the distances.

7.1 GMOS observation and data reduction

The selected UCDs were observed using the 8-m Gemini-South telescope with the Gemini Multi-Object Spectrograph (GMOS; Hook et al. 2004). The observations were carried out through the months of September to December 2019 as part of the programs GS-2019B-Q-230 (band 2) and GS-2019B-Q-312 (band 3). We used GMOS with the R150 grating and the OG515 blocking filter to deliver a R~600 resolution, across the 7000–10 000 Å; range. For all targets, three spectra, centered at 7900, 8000, 8100 Å; at z' filter were taken for each source, to cover the small gaps between the three GMOS detectors, and a focal plane unit of 1 arcsec was selected. We binned both in spatial and spectral direction to 4x4 pixels to increase our signal-to-noise (SNR) ratio. For every change in central wavelength, a flat and a CuAr frame was taken immediately following the science exposure. Table 6 shows the observation log for all the objects observed with GMOS. The individual spectra for the same source were rebinned preserving flux and combined into a single coadded spectrum using standard routines. The typical SNR per pixel for the coadd spectra is ~ 6.

The objects UCD 1, UCD 3, UCD 10, and UCD 8 are wide binary systems candidates presented previously in dal Ponte et al. (2020) as composed by two L dwarfs. As an observation strategy, we place both objects (L dwarfs) of each system on a single long-slit to obtain two spectra at the same time. The data reduction was carried out using the standard GMOS pipeline contained in the GEMINI IRAF/PYRAF package. The basic steps include bias subtraction, flat-field correction, and wavelength calibration and for the extraction of the spectra we use the APALL pipeline. The spectra have not been flux calibrated and corrected for telluric absorption.

7.2 Ultracool dwarfs spectral types

To determine the spectral type for our UCDs we use a simple χ^2 minimization relative to templates taken from Kirkpatrick et al. (1999). The templates were smoothed down and rebinned to match our resolution and wavelength range of 7200–9400 Å;. We also visually inspected the five best-fitting templates to check the accuracy of the fit. For the instrumental fluxes, we attributed a Poisson fluctuation in the detector counts for every λ. We also multiplied

Table 6. Observation log of the selected ultracool dwarfs.

Name	Obs. Date	Airmass	λ (Å)	Exp. Time
		GS-2019B-Q-230		
UCD 10	2019-09-30	1.35	7900	30.0
	2019-10-07	1.37	7900	30.0
	2019-10-07	1.28	8000	45.0
	2019-10-07	1.22	8100	42.0
UCD 1	2019-10-07	1.16	7900	30.0
	2019-10-07	1.25	8000	68.8
	2019-10-07	1.25	8100	42.0
UCD 3	2019-11-30	1.06	7900	30.0
	2019-11-30	1.07	8000	45.0
	2019-11-30	1.12	8100	42.0
UCD 11	2019-12-01	1.36	7900	26.6
	2019-12-01	1.50	8000	30.0
	2019-12-01	1.73	8100	40.0
		GS-2019B-Q-230		
UCD 36	2019-09-04	1.36	7900	60.0
	2019-09-04	1.21	8000	60.0
	2019-09-04	1.16	8100	45.0
UCD 8	2019-09-22	1.38	7900	30.0
	2019-09-28	1.33	8000	30.0
	2019-09-28	1.25	8100	30.0
UCD 6	2019-09-30	1.17	7900	60.0
	2019-09-30	1.12	8000	22.16
	2019-10-06	1.22	8000	30.0
	2019-10-08	1.26	8100	45.0
UCD 12	2019-10-06	1.13	7900	60.0
	2019-11-20	1.13	8000	15.0
	2019-11-21	1.11	8000	45.0
	2019-11-21	1.11	8100	45.0

Note. The central wavelength is in Å; and the exposure time in minutes.

the templates by a normalization factor before comparing them to each UCD spectrum. This normalization factor is given by

$$N = \frac{\int_{\lambda_1}^{\lambda_2} Flux_{\text{spectra}}}{\int_{\lambda_1}^{\lambda_2} Flux_{\text{template}}},$$

where the integrals in the numerator and denominator are over the instrumental fluxes of GMOS and template spectra, respectively, within the spectral range of our analysis (λ = 7200–9400 Å).

Fig. 10 shows the spectra and the lowest χ^2 template, along with this best match spectral type. Table 7 shows the photo-type estimated in Carnero Rosell et al. (2019) and the new photo type estimation as presented earlier. The photo-type previously estimated has an typical uncertainty of one or two types due to the method adopted. As discussed previously, to obtain photometric distances we compared the photo-type with our empirical model grid to estimate the absolute magnitude and then obtained the distance modulus for each object. Following the same methodology, but now using the spectral type estimated from the template fitting, new distances were calculated and are shown in the last column of Table. UCD 1, UCD 3, and UCD 10 remain wide binary candidates based on the new distances measurements whereas UCD 8 is discarded as a common distance pair. This latter, in fact, is an interesting pair of sources. Their apparent magnitudes are quite similar in most filters and they are about 1 arcmin apart from each other on the sky. Their proper motion information comes from the CatWISE catalogue and is not precise enough to help assessing the nature of the pair. On the other hand, their Gemini/GMOS spectra are best fitted by an M8 and L0

template, respectively for the a and b components. In Appendix A we compare their spectra to other similar templates, showing the difficulty in attributing a spectral type with precision better than ±2 in some cases.

Also, the comoving candidate systems still have large uncertainties in their proper motion measurements, rendering current kinematical information not an efficient diagnostic. The spectra presented in this section are a basic sanity check that we are in fact selecting ultracool dwarfs and our method to estimate spectral types works as expected, with an accuracy of ±2 types.

8 CONCLUSIONS

Using the recent Dark Energy Survey data release (DR2) combined with VHS DR6, VIKING DR5, and AllWISE data, we were able to identify new ultracool dwarfs candidates, probing faint and more distant objects than those presented in the literature so far. We select these candidates based on their colours (i–z), (z–Y), and (Y–J) up to $z \leq 23$. We applied a classification method where a photo-type can be attributed to each object based only on its photometry. Here we have presented updated colour templates in our classification scheme compared to previous work in Carnero Rosell et al. (2019), and expanded the ultracool dwarf candidate sample to cover almost the entire DES footprint area, thanks to the new VHS DR6 catalogue.

In total, our new sample has 19 583 ultracool dwarf candidates, where 14 099 are presented here for the first time. The complete sample includes 142 spectroscopically confirmed objects from the literature, plus 5342 ultracool dwarf candidates from the literature, where the vast majority (5257 candidates) are from our previous work. The samples from the literature, both with spectroscopic confirmation and candidates were used here as a validation to our method. The method to infer the spectral type consists in a minimization of the χ^2 relative to empirical templates of M, L, and T dwarfs. The comparison between our estimated photo-type with those from the literature showed us that our photo-type is accurate in ±2 spectral types. During the classification step, we also used LEPHARE code with templates from galaxies and quasars in order to identify extragalactic contamination and remove those sources from our final sample.

Our L and T candidates comprise the largest such sample as of today. For instance, Skrzypek et al. (2016) report on finding 1361 L and T dwarfs brighter than J = 17.5 within an effective area of 3070 deg^2 in the Northern Hemisphere. Their UCDs span distances out to 150 pc, whereas our sample goes at least three times farther, out to ∼ 500 pc, and covers a solid angle 60 per cent larger. This much larger volume, coupled with the exponential drop in density in the Galactic disk at the high latitudes we cover, make the two samples quite consistent in terms of the number of objects found.

We also show some applications for our new ultracool dwarf candidates: (i) search for new candidate members to YMG and associations; (ii) photometric variable objects; (iii) search for new wide binary candidate systems. For the first application, we used the BANYAN Σ algorithm to investigate the likelihood of each object in our sample being a member of a YMG. We found 20 new candidate members with membership probability > 90 per cent. We also identify 291 variable candidate sources in our sample, of which 10 per cent are young objects. Also, a higher percentage of the variable sample is concentrated in the L9–T3 range. In addition, as presented previously in dal Ponte et al. (2020), we search for wide binary systems composed of two ultracool dwarfs and here we present four new candidate systems.
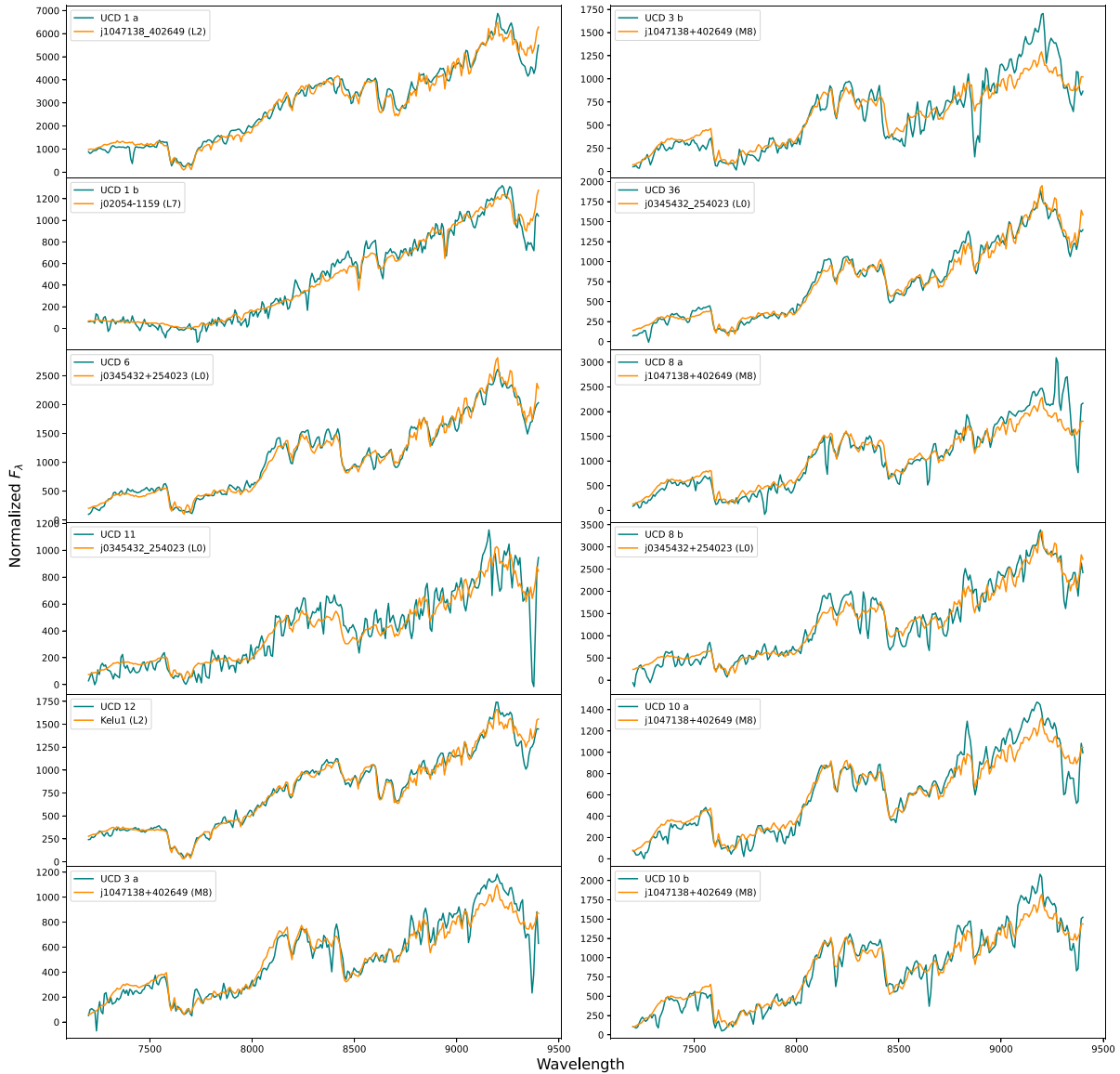
Figure 10. UCD spectra (blue) and the best-fitting template (orange), ordered by right ascension. The fluxes shown are relative F_λ in arbitrary units. The flux of the templates was multiplied by a normalization factor prior to the fit, as explained previously. The individual members of the wide binary candidates are identified by *a,b* labels.

Table 7. Objects z magnitude, photo-type, spectral type, and photometric distances.

Name	RA	DEC	Ph.T		Sp. Type	z	Distance	
UCD 6	10.642	−3.531	L0∗	L0	L0	20.24 ± 0.01	195 ± 33∗	176 ± 17
UCD 11	21.102	−44.986	L2∗	L1	L0	20.92 ± 0.02	173 ± 8∗	219 ± 22
UCD 12	22.886	−5.240	L2∗	L1	L2	20.83 ± 0.01	158 ± 9∗	149 ± 15
UCD 36	321.070	0.484	L0∗	M9	L0	20.63 ± 0.01	246 ± 10∗	222 ± 21
UCD 1 a	0.876	−0.216	L2∗	L1	L2	19.17 ± 0.01	74 ± 2∗	70 ± 6
UCD 1 b	0.876	−0.185	L7∗	L8	L7	21.15 ± 0.02	70 ± 7∗	64 ± 6
UCD 3 a	74.456	−49.567	L0∗	M9	M8	20.96 ± 0.02	349 ± 22∗	429 ± 50
UCD 3 b	74.455	−49.565	L0∗	M9	M8	21.13 ± 0.02	371 ± 29∗	457 ± 49
UCD 8 a	349.952	−52.073	L0∗	M9	M8	19.94 ± 0.01	181 ± 7∗	268 ± 26
UCD 8 b	349.929	−52.065	L0∗	M9	L0	19.95 ± 0.01	176 ± 5∗	160 ± 15
UCD 10 a	355.516	−61.588	L0∗	M9	M8	20.78 ± 0.01	279 ± 29∗	416 ± 41
UCD 10 b	355.533	−61.595	L0∗	L0	M8	21.17 ± 0.02	286 ± 29∗	445 ± 48

Note. The photo-type and the distance column is divided into Carnero Rosell et al. (2019) and new measurements as presented in the earlier sections. All the estimates provided by Carnero Rosell et al. (2019) have ∗ mark.

Finally, we show here the spectroscopic confirmation of 12 new ultracool dwarfs, a basic sanity check of our selection and classification method.

DATA AVAILABILITY

Data underlying this article are available in https://des.ncsa.illinois.edu/releases/other/Y6-LTdwarfs.

REFERENCES

Abbott T. M. C. et al., 2021, ApJS, 255, 20
Arnouts S., Cristiani S., Moscardini L., Matarrese S., Lucchin F., Fontana A., Giallongo E., 1999, MNRAS, 310, 540
Barenfeld S. A., Bubar E. J., Mamajek E. E., Young P. A., 2013, ApJ, 766, 6
Bate M. R., Bonnell I. A., 2005, MNRAS, 356, 1201
Bell C. P. M., Mamajek E. E., Naylor T., 2015, MNRAS, 454, 593
Best W. M. J. et al., 2018, ApJS, 234, 1
Best W. M. J. et al.., 2020, The UltracoolSheet: Photometry, Astrometry, Spectroscopy, and Multiplicity for 3000 + Ultracool Dwarfs and Imaged Exoplanets. Available at: https://doi.org/10.5281/zenodo.4169085
Billères M., Delfosse X., Beuzit J. L., Forveille T., Marchal L., Martín E. L., 2005, A&A, 440, L55
Bochanski J. J., Hawley S. L., Covey K. R., West A. A., Reid I. N., Golimowski D. A., Ivezić Ž., 2010, AJ, 139, 2679
Burgasser A. J. et al., 2002a, ApJ, 564, 421
Burgasser A. J., Marley M. S., Ackerman A. S., Saumon D., Lodders K., Dahn C. C., Harris H. C., Kirkpatrick J. D., 2002b, ApJ, 571, L151
Carnero Rosell A. et al., 2019, MNRAS, 489, 5301
Cruz K. L. et al., 2007, AJ, 133, 439
Cushing M. C. et al., 2011, ApJ, 743, 50
Cutri R. M. et al., 2013, Explanatory Supplement to the AllWISE Data Release Products, Explanatory Supplement to the AllWISE Data Release Products. Available at: http://wise2.ipac.caltech.edu/docs/release/ allwise/expsup
dal Ponte M. et al., 2020, MNRAS, 499, 5302
Day-Jones A. C. et al., 2013, MNRAS, 430, 1171
Dhital S., Burgasser A. J., Looper D. L., Stassun K. G., 2011, AJ, 141, 7
Dhital S., West A. A., Stassun K. G., Schluns K. J., Massey A. P., 2015, AJ, 150, 57
Dupuy T. J., Liu M. C., 2012, ApJS, 201, 19
Edge A., Sutherland W., Kuijken K., Driver S., McMahon R., Eales S., Emerson J. P., 2013, Messenger, 154, 32
Epchtein N. et al., 1997, Messenger, 87, 27
Faherty J. K., Burgasser A. J., West A. A., Bochanski J. J., Cruz K. L., Shara M. M., Walter F. M., 2010, AJ, 139, 176
Faherty J. K. et al., 2012, ApJ, 752, 56

Faherty J. K. et al., 2016, ApJS, 225, 10
Flaugher B. et al., 2015, AJ, 150, 150
Fontanive C., Biller B., Bonavita M., Allers K., 2018, MNRAS, 479, 2702
Gagné J. et al., 2015, ApJS, 219, 33
Gagné J. et al., 2018, ApJ, 856, 23
Gaia Collaboration, 2022, preprint (arXiv:2208.00211)
Hook I. M., Jørgensen I., Allington-Smith J. R., Davies R. L., Metcalfe N., Murowinski R. G., Crampton D., 2004, PASP, 116, 425
Ilbert O. et al., 2006, A&A, 457, 841
Kiman R., Schmidt S. J., Angus R., Cruz K. L., Faherty J. K., Rice E., 2019, AJ, 157, 231
Kirkpatrick J. D. et al., 1999, ApJ, 519, 802
Kirkpatrick J. D., Barman T. S., Burgasser A. J., McGovern M. R., McLean I. S., Tinney C. G., Lowrance P. J., 2006, ApJ, 639, 1120
Kirkpatrick J. D. et al., 2021a, ApJS, 253, 7
Kirkpatrick J. D. et al., 2021b, ApJ, 915, L6
Kiwy F. et al., 2022, AJ, 164, 3
Kota T. et al., 2022, AJ, 163, 116
Lawrence A. et al., 2007, MNRAS, 379, 1599
Leggett S. K. et al., 2010, ApJ, 710, 1627
Luhman K. L., 2012, Araa, 50, 65
Luhman K. L., Stauffer J. R., Mamajek E. E., 2005, ApJ, 628, L69
Lyke B. W. et al., 2020, ApJS, 250, 8
McMahon R. G., Banerji M., Gonzalez E., Koposov S. E., Bejar V. J., Lodieu N., Rebolo R., VHS Collaboration, 2013, Messenger, 154, 35
Marocco F. et al., 2021, ApJS, 253, 8
Meisner A. M. et al., 2021, ApJ, 915, 120
Metchev S. A. et al., 2015, ApJ, 799, 154
Murphy S. J., Lawson W. A., 2015, MNRAS, 447, 1267
Naud M.-E., Artigau É., Doyon R., Malo L., Gagné J., Lafrenière D., Wolf C., Magnier E. A., 2017, AJ, 154, 129
Nidever D. L. et al., 2021, AJ, 161, 192
Radigan J., 2014, ApJ, 797, 120
Reipurth B., Clarke C., 2001, AJ, 122, 432
Reylé C., 2018, A&A, 619, L8
Riedel A. R., Blunt S. C., Lambrides E. L., Rice E. L., Cruz K. L., Faherty J. K., 2017, AJ, 153, 95
Ryan R. E., J., Hathi N. P., Cohen S. H., Windhorst R. A., 2005, ApJ, 631, L159
Schmidt S. J., Hawley S. L., West A. A., Bochanski J. J., Davenport J. R. A., Ge J., Schneider D. P., 2015, AJ, 149, 158
Schmidt S. J. et al., 2019, ApJ, 876, 115

Shkolnik E. L., Allers K. N., Kraus A. L., Liu M. C., Flagg L., 2017, AJ, 154, 69
Skrutskie M. F. et al., 2006, AJ, 131, 1163
Skrzypek N., Warren S. J., Faherty J. K., Mortlock D. J., Burgasser A. J., Hewett P. C., 2015, A&A, 574, A78
Skrzypek N., Warren S. J., Faherty J. K., 2016, A&A, 589, A49
Smith L., Lucas P. W., Burningham B., Jones H. R. A., Smart R. L., Andrei A. H., Catalán S., Pinfield D. J., 2014, MNRAS, 437, 3603
Softich E. et al., 2022, ApJ, 926, L12
Sorahana S., Nakajima T., Matsuoka Y., 2019, ApJ, 870, 118
Stassun K. G. et al., 2018, AJ, 156, 102
Stringer K. M. et al., 2021, ApJ, 911, 109
Ujjwal K., Kartha S. S., Mathew B., Manoj P., Narang M., 2020, AJ, 159, 166
Vos J. M. et al., 2019, MNRAS, 483, 480
Wenger M. et al., 2000, A&AS, 143, 9
West A. A. et al., 2011, AJ, 141, 97
Wright E. L. et al., 2010, AJ, 140, 1868
Zuckerman B., Bessell M. S., Song I., Kim S., 2006, ApJ, 649, L115

APPENDIX: UCD 8 OBJECTS TEMPLATE FITTING

In assessing the nature of binary system candidates involving one or more UCD, it is important to take into account the uncertainties in assigning a spectral type, since our photometric distances are based on template absolute magnitudes for each type. We show here the interesting example of the pair made by UCD 8, for which we obtained Gemini/GMOS spectra of the UCD 8a and UCD 8b candidate members. Fig. A1 we show these spectra along with the templates for M8, M9 and L0. The M8 and M9 templates fit the spectra in a very similar way. The L0 template seems to be the best fit for the UCD 8 b, while for the UCD 8 a, the M8 has the lowest χ^2. As mentioned in Section 7, these two sources are particularly interesting since the objects have very similar magnitudes in all bands and we could expect a more similar spectral type. Because the assigned spectral types differ by two units, however, their distances are now inconsistent with a physical pair. More accurate distance estimates, as well as proper motions, will be required to resolve their nature.
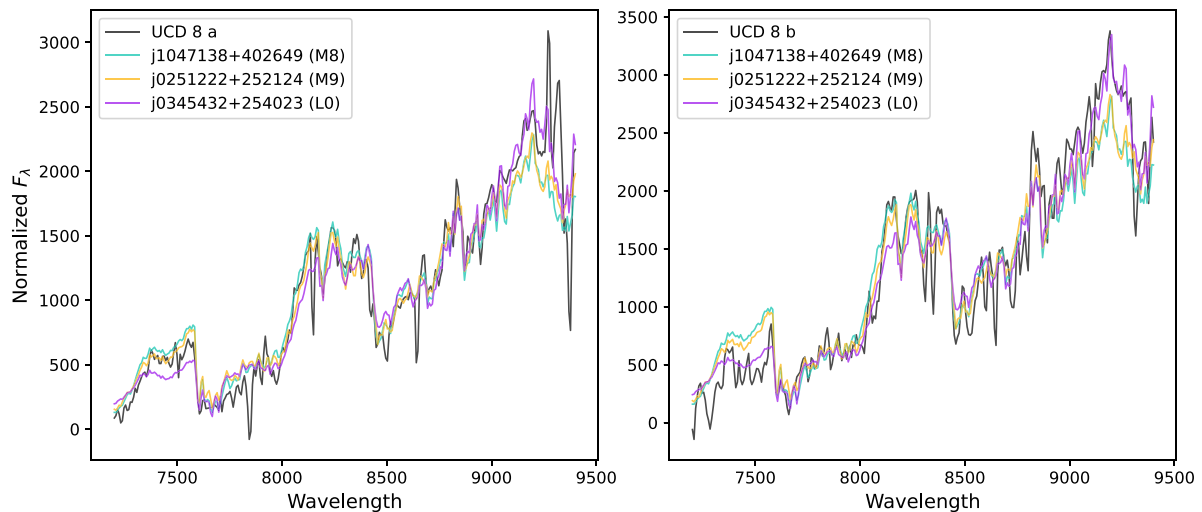
Figure A1. UCD spectra (black) and the M8 (green), M9 (yellow) and L0 (purple) templates. The fluxes shown are relative F_λ in arbitrary units. As in Fig. 10, the flux of the templates was multiplied by a normalization factor.